



Influence of liquid water accumulation on the impedance of a PEM fuel cell operating in dead end mode: Physical modeling and experimental validation

Majid Shateri ^{a,*}, Farschad Torabi ^b

^a Department of Energy Systems, Faculty of Mechanical Engineering, K.N. Toosi University of Technology, Tehran, Iran

^b Battery and Energy Generators Research Lab, Faculty of Mechanical Engineering, K.N. Toosi University of Technology, Tehran, Iran

ARTICLE INFO

Keywords:

PEM fuel cell
Dead-end mode
Liquid water saturation
Electrochemical impedance spectroscopy
Physical modeling
Experimental validation

ABSTRACT

The dead-end mode operation of a PEM fuel cell reduces the reactants consumption and the system's complexity, but also decreases its performance due to the accumulation of liquid water, which must be purged periodically. Despite extensive use of the EIS technique in studying PEM fuel cells' internal processes, the inherently transient nature of dead-end mode operation has challenged the application and interpretation of this technique. In this paper, a novel analytical model is proposed to physically investigate the effect of liquid water accumulation on the impedance of a PEM fuel cell in dead-end mode operation. The model is well validated against experimental polarization curves and impedance diagrams in various operating conditions by employing a two-step fitting procedure. The findings of the model indicate the constant presence of a large amount of liquid water in the fuel cell due to the dead-end operation. Additionally, the buildup of liquid water reduces the active area of the catalyst layer and the effective oxygen diffusion coefficient in GDL, increasing both the charge and mass transfer resistances. Finally, with its low computational cost, the developed analytical model can provide a suitable framework for purposes such as fault diagnosis and degradation prognosis.

1. Introduction

Overcoming the current energy situation caused by the high consumption of fossil fuels requires a serious determination to move towards alternative energy sources. For more than three decades now, hydrogen and fuel cell technologies have become an alternative solution to achieving a sustainable and clean energy system globally, and recent advances in cost and performance have increased their economic justification. Hydrogen fuel cells are electrochemical converters that directly convert hydrogen and oxygen into electricity. This electrochemical reaction allows the production of high-efficiency electrical energy through a non-combustion process without CO₂ emissions. Due to this, many countries are developing hydrogen fuel cell technologies for transportation and fixed/portable power generation applications [1–3].

In general, whether or not the gas flow field outlet is blocked, two general methods are formed to feed the fuel and oxidant: “dead-end” and “open-end” modes. In the latter case, the fuel (hydrogen) and oxidant (oxygen or air) are supplied at a higher rate than is required for the reaction. The excess gas flow, in turn, expels the water produced during the reaction by the convective force. To maximize fuel utilization, unreacted residual gases must be re-transferred to the fuel cell inlet using a recirculation system, resulting in an increased pressure

drop and power consumption in the fuel cell. This ultimately affects the overall efficiency of the system. On the opposite side, in the former case, the system is a closed-end, which aims to increase the efficiency of fuel consumption by considering the stoichiometric coefficient of the inlet gases close to one. The result of this feeding method is the removal of blowers and the recirculation part from the reactants supply circuit, reducing the power consumption of the auxiliary systems and, of course, reducing the complexity of the fuel cell system. Contrary to these advantages, closing the outlet causes the accumulation of liquid water in channels and porous medium. This can cause local fuel and oxidant starvation, which in turn will lead to a voltage drop. In order to achieve stable performance, it is necessary to recover the fuel cell by opening the outlets and draining the liquid water. However, small amounts of reacting gases are also released during the purging process. Therefore, the number of recovering cycles should be minimized for safety and maximum fuel efficiency [4–7].

Despite excellent capabilities to complement or even replace conventional fossil fuel-based energy systems, dead-end PEMFCs have not yet reached full maturity in the commercialization phase. Issues such as managing liquid water accumulation [7], MEA degradation [8], purging process [9], and optimal stack design [10] are essential topics of interest to researchers and scientists. Among these, liquid water

* Corresponding author.

E-mail addresses: m.shateri@mail.kntu.ac.ir (M. Shateri), ftorabi@kntu.ac.ir (F. Torabi).

<https://doi.org/10.1016/j.electacta.2023.141940>

Received 24 September 2022; Received in revised form 16 January 2023; Accepted 23 January 2023

Available online 25 January 2023

0013-4686/© 2023 Elsevier Ltd. All rights reserved.

Nomenclature

| | |
|-----------|---|
| R | Universal gas constant ($\text{J K}^{-1} \text{mol}^{-1}$) |
| F | Faraday's constant (C mol^{-1}) |
| A | Proportionality coefficient (C cm^{-2}) |
| C | Molar concentration (mol cm^{-3}) |
| C_{dl} | Double-layer capacitance (F cm^{-2}) |
| D | Diffusion coefficient ($\text{cm}^2 \text{s}^{-1}$) |
| E_{OCV} | Open circuit potential (V) |
| f | Frequency (Hz) |
| i | Imaginary unit (–) |
| j | Current density (A cm^{-2}) |
| M | Molecular weight (Kg mol^{-1}) |
| N | Number of moles (mol) |
| n | Number of electrons participating in the electrode reaction (–) |
| P | Inlet pressure (MPa) |
| R | Electrical resistance ($\Omega \text{ cm}^2$) |
| RH | Relative humidity (%) |
| S | Surface area (cm^2) |
| s | Saturation (–) |
| T | Operating temperature (K) |
| t | Time (s) |
| U | Cell potential (V) |
| V | Geometric volume (cm^3) |
| Z | Electrical impedance ($\Omega \text{ cm}^2$) |

Greek Symbols

| | |
|------------|--|
| α | Charge transfer coefficient (–) |
| δ | Layer thickness (m) |
| η | Over-potential (V) |
| γ | Reaction order (–) |
| ω | Angular velocity (rad s^{-1}) |
| ϕ | Free parameter (–) |
| ρ | Density (Kg m^{-3}) |
| τ | Tortuosity factor (–) |
| ϵ | Free porosity (–) |

Subscripts

| | |
|----------------------|-------------------------------------|
| act | Active area |
| diff | Related to diffusion value |
| ohm | Ohmic value |
| top | Top point |
| C | Capacitive value |
| ct | Related to charge transfer value |
| e | Electrode |
| ex | Related to exchange current density |
| F | Faradic value |
| GDL | Gas diffusion layer |
| H_2O | Water |
| O_2 | Oxygen |
| sat | Related to saturation value |
| T | Total value |

Superscripts

| | |
|-----|-------------------------------------|
| – | Steady-state value |
| 0 | Standard condition |
| ~ | Oscillating value |
| eff | Effective value in GDL porous media |
| in | Inlet |
| sat | Saturation condition |

water issue in this type of PEMFC [11]. Researchers utilize various experimental methods to study water dynamics and management in fuel cells. Rahimi et al. [9] used direct visualization as a reliable and cost-effective method to investigate the dead-end operation, while Chevalier et al. [12] and Siegel et al. [13] employed more complicated synchrotron X-ray radiography and Neutron imaging methods for this purpose.

While the above techniques are all laboratory-based and unsuitable for practical diagnostic purposes, electrochemical impedance spectroscopy (EIS) has introduced itself as an in-situ and non-invasive method used widely to study different aspects of PEM fuel cells [14]. However, the application of EIS for analysis of dead-end mode condition has been highly limited due to the transient nature of the system and the consequent voltage reduction, which may disturb the stability of the PEMFC. The lowest frequency that can be recorded regarding the system's dynamics is the source of the mentioned limitation of the standard EIS technique. A 0.01 Hz frequency, for example, necessitates stability over at least 100 s for only a single measurement cycle. The test period for a complete sweep comprising many frequency points gets so long that only steady-state systems can retain the required stability [15]. Only few works have been published in the literature to overcome this issue in EIS measurements of a dead-ended PEMFC. Strahl et al. [16] proposed a “fast” EIS test procedure from 10 kHz to 10 Hz, which requires only about 20 s to quantify the water-related performance challenges in a PEMFC operating with dead-end anode. They chose low current densities (0.04 and 0.09 A/cm²) to minimize the voltage drop during the test to only a few millivolts. Recently, a method based on AC impedance measurement was introduced by Ge et al. [17] to detect cathode corrosion in a dead-ended PEMFC, in which they calculated polarization resistances using only two anode-sensitive frequency points obtained over a 2-second sampling period.

A novel technique for acquiring entire EIS spectra during a dead-ended operation has been developed by Meyer et al. [15], wherein a distinct frequency was measured during each cycle. Then, the new “reconstructed impedance” method integrates the outputs of the successive cycles to construct the whole EIS of the dead-ended operation. Indeed the repeatability of the dead-end and purge processes makes it possible to consider the test at each frequency to be in a pseudo-steady-state in this scenario. Based on the reconstructed impedance test method, Asghari et al. [18] investigated the performance of a dead-ended anode single-cell PEMFC under various operating temperatures, air stoichiometries, and purge intervals.

Besides experimental studies, the physical modeling of the PEMFCs provides a convenient and cost-effective tool for understanding the internal processes that are not easily detectable through experimental observations. In addition, the modeling is an essential step in condition monitoring, fault detection, and controller design of fuel cell systems. So far, all models in the field of PEMFCs with dead-end operating condition have been published based on the time domain approach, and the authors have not identified any work in the associated literature based on the frequency domain and physical impedance modeling. The rationale stems from the challenges and complexities of executing the EIS test in dead-end mode, which has resulted in few experimental outcomes in this area. This, in turn, is attributable to the system's dynamics

accumulation can be considered the root cause of the other problems in a dead-end fuel cell, as it causes a performance loss in the short-term and MEA degradation in the long-term duration. Also, the purpose of the purging process and cascade stack design is to manage the excess

due to the liquid water accumulation in a confined environment. As a result, it is vital to account for the influence of liquid water formation and buildup while modeling the impedance of a PEMFC working in dead-end mode. Accordingly, the primary contribution of this study is to propose a physical model for the impedance of a dead-end PEMFC, in which the influence of liquid water accumulation is regarded through a transient equation of saturation level. As the water formation occurs on the cathode side, its related water management issues are more significant than those for the anode. Thus, the model concentrates on the study of dead-end operation of the cathode side of a H_2/O_2 PEMFC. The suggested model is one-dimensional and considered to be isothermal due to the short period of EIS test procedure, and has been solved analytically. Furthermore, the validity of the developed model is confirmed by experimental tests. Then, the effect of saturation level variation on the impedance diagram will be discussed. In summary, the following are the paper's innovations: 1. introducing a physical model for the impedance of a PEMFC operating in dead-end mode, 2. incorporating the impact of liquid water saturation in the impedance model, 3. experimental measurements of the impedance of a dead-end PEMFC and validation of the physical model against the test results, 4. investigating the effect of the saturation level variation on the impedance diagram.

The content of the rest of the article is set as follows: The method and equipment used in the experiments are described in Section 2. Section 3 is organized into three subsections. First, the governing equations of the problem are stated in the time domain. Then, their equivalents in the frequency domain are developed. Finally, the physical model is extracted through an analytical solution. After validating the model and estimating the unknown parameters, Section 4 examines the effect of saturation level variation on the impedance diagram. The last section is dedicated to conclusions and introducing possible applications.

2. Experimental

A 3 cell PEMFC stack with 500 cm^2 active area was assembled in this study (Fig. 1(a)) in order to verify the validity and accuracy of the developed model through measuring electrochemical impedance spectra (EIS) and polarization curves (V-I curves) at different operating conditions. High-purity H_2 and O_2 (99.99%) gases were used to feed the stack at flow rates of 6.8 SLPM on the anode and 3.4 and 2.5 SLPM on the cathode. For hydrogen, it correlates with a stoichiometric ratio of 1.5, and for oxygen, with 1.5 and around 1.1 during open-end and dead-end operations, respectively. Table 1 lists the fuel cell operating temperatures, inlet gauge pressures, and other test conditions. To explore the influence of cathode water accumulation on the impedance diagram, the anode operated in open-end mode with a relative humidity of 100% throughout the experiment to preserve its water balance and have the most negligible effect on the fuel cell's impedance. The MEA used is a PaxiTech product that comprises a $50\text{ }\mu\text{m}$ thick Nafion membrane with a platinum loading of $0.5\text{ mg}/\text{cm}^2$ as a catalytic coating on both the anode and cathode sides. In addition, SGL carbon paper (uncompressed thickness of $325\text{ }\mu\text{m}$ and free porosity of 52% according to the manufacturer's documentation) was employed as GDLs, which also equipped with a 5% wt. PTFE to enhance its hydrophobicity characteristics. The MEA and the GDLs were sandwiched between graphite bipolar plates with a 1 MPa clamping pressure. A new parallel serpentine flow field pattern, which has been introduced by Ref. [9], was employed for the anode and cathode sides (Fig. 1(b)). The PEMFC stack utilized a water-cooling system managed by a PID controller. As a result, the temperature difference between inlet and outlet of the stack was measured by thermocouples during the whole experiment and not permitted to be more than 1 K.

The test station was equipped with two bubble humidifiers and guaranteed the full humidification of the dry inlet gases by setting the humidification temperature to the cell's operating temperature. The experiments were conducted using an Autolab potentiostat along with a

Table 1

Varying operating conditions for polarization and impedance test cases.

| Test | Num. | <i>P</i> (bar g) | <i>T</i> (K) | <i>RH</i> (%) An./Cath. | Stoi. An./Cath. | Oper.Mode An./Cath. |
|------|------|------------------|--------------|----------------------------|--------------------|------------------------|
| V-I | 1 | 1 | 313.15 | 100/100 | 1.5/1.5 | Open/Open |
| V-I | 2 | 2 | 313.15 | 100/100 | 1.5/1.5 | Open/Open |
| V-I | 3 | 2 | 333.15 | 100/100 | 1.5/1.5 | Open/Open |
| EIS | 1 | 1 | 313.15 | 100/100 | 1.5/1.1 | Open/Dead |
| EIS | 2 | 2 | 313.15 | 100/100 | 1.5/1.1 | Open/Dead |
| EIS | 3 | 2 | 333.15 | 100/100 | 1.5/1.1 | Open/Dead |

Chroma electronic load to automatically record and control the current and voltage evolutions. The V-I curves were recorded at a low current sweep rate of 1 A per 2 s, which maintains the pseudo-steady-state of the system. Cell 3 (the output cell) has a more considerable voltage drop than the other two cells due to the more significant impacts of water accumulating at the end of the stack (Fig. 3). Accordingly, this cell was chosen as a purge cell, and impedance measurements were recorded for it in a galvanostatic mode and at a DC current of $0.4\text{ A}/\text{cm}^2$. The AC current amplitude was considered to be 5% of DC one. The frequency range during the EIS test was from 1 kHz to $\sim 1\text{ Hz}$. LabView software was employed for monitoring and controlling the test station performance. The Process flow diagram (PFD) of the utilized in-house test station is illustrated in Fig. 2.

Following the work of Meyer et al. [15], we measured the impedance at each frequency point in a separate dead-end operation interval, starting all of them immediately after closing the purge valve (Fig. 4). Then, the impedance spectrum was reconstructed by combining together the results of all of the points in the frequency range.

3. Theoretical paradigm of the model

Fig. 5 shows the schematic of the modeling domain, which consists of a surface electrode separated from the cathode channel by a porous diffusion medium (GDL). An analytical impedance model based on the physico-chemical governing equations is developed to predict the frequency response of a PEMFC operating in dead-end mode to an AC excitation signal in the presence of liquid water saturation, which to the best knowledge of the authors has not been studied beforehand. The main hypotheses of the model are as follows [19–21]:

1. The gas in the GDL is assumed to be an ideal mixture, and its diffusion obeys Fick's law.
2. Due to the faster kinetic and diffusion processes of hydrogen with regard to oxygen in a PEMFC, the impedance of the anode side can be neglected compared to that of the cathode.
3. The operating temperature of the cell is considered to be constant. Also, it is usual to supply the inlet flow of the cathode by 100% relative humidity to ensure the membrane full hydration. This causes the water vapor pressure to be fixed to its saturation value at cell temperature.
4. The catalyst layer is treated as a surface where the electrochemical reactions take place.
5. The membrane effect is only ohmic with a constant resistivity because its water content remains unchanged due to relatively short time intervals among two consecutive purges.

EIS method needs stability of the system during the test, but purging process in dead-end mode operation disturbs it. Therefore, the model has to be confined to the PEMFC operation between two consecutive purges.

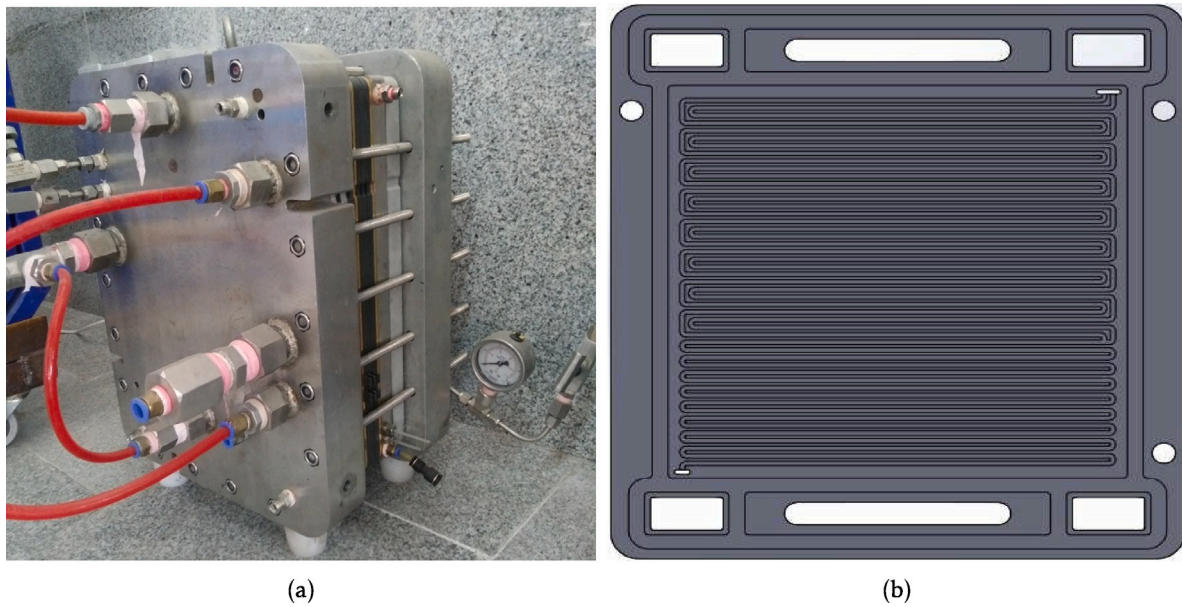


Fig. 1. (a). The 3 cell cathode dead-ended H₂/O₂ stack with 500 cm² active area. (b). Descending parallel serpentine flow field pattern.

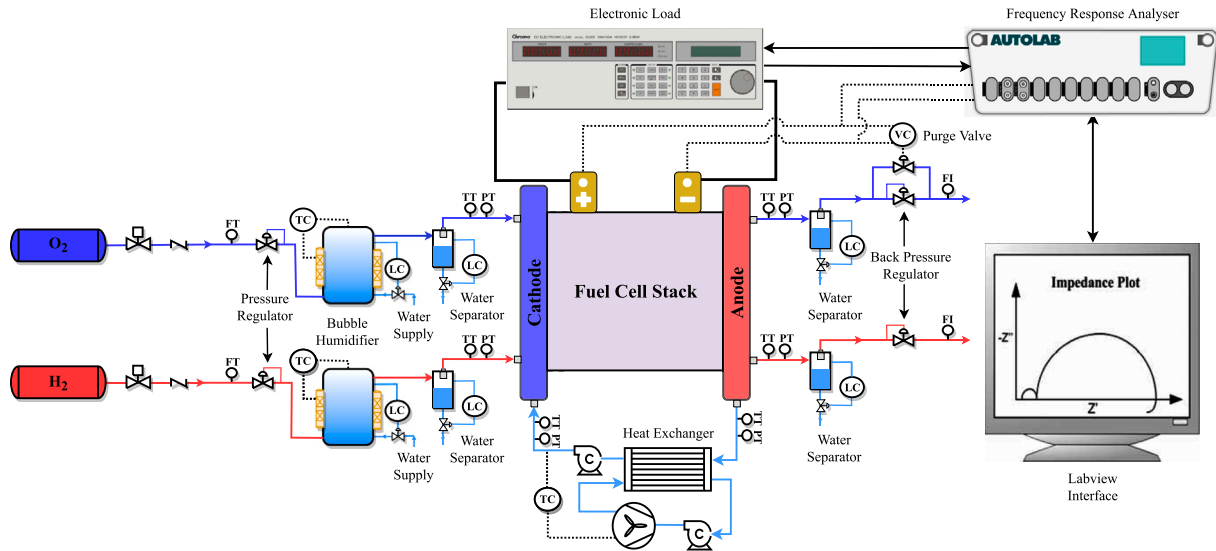


Fig. 2. Process flow diagram of the fuel cell test station.

3.1. Governing equations in time domain

3.1.1. Liquid water saturation equation

Being humidified by 100%, the inlet flow of the cathode is saturated; therefore, the generated water due to electrochemical reaction will be present in condensed form. The governing equation of the liquid water in GDL can be derived as a function of Faradic current [21]:

$$\left(\frac{\rho}{M}\right)_{\text{H}_2\text{O}} \epsilon V_{\text{GDL}} \frac{ds}{dt} = \frac{j_F S_{\text{act}}}{2F} \quad (1)$$

where s stands for the saturation in the GDL defined as the fraction of a GDL pores volume occupied by liquid water. The presence of liquid water causes a decrease in the available active surface area S_e of electrode. This effect is considered through the ratio of the parameter's nominal value proportional to the liquid water saturation:

$$S_{\text{act}} = S_e (1 - s) \quad (2)$$

As a result of inserting Eq. (2) into Eq. (1), the liquid water saturation equation in GDL takes the following form, in which all the physical

constants are gathered in the parameter A :

$$A \frac{ds}{dt} = j_F (1 - s) \quad (3)$$

$$A = \left(\frac{\rho}{M}\right)_{\text{H}_2\text{O}} \epsilon V_{\text{GDL}} \frac{2F}{S_e}$$

3.1.2. Oxygen species equation

The transport of oxygen species in the cathode GDL obeys Fick's law of diffusion as follows:

$$\frac{dC_{\text{O}_2}}{dt} = \frac{d}{dx} \left(D_{\text{O}_2}^{\text{eff}} \frac{dC_{\text{O}_2}}{dx} \right) \quad (4)$$

where superscript "eff" of diffusion coefficient denotes the effective diffusivity of the oxygen species in the porous media, which is calculated through the Bruggemann correlation [22] to account for the effects of porosity and tortuosity. Furthermore, the superscript "eff" of porosity is due to the effect of liquid water accumulation in GDL pores:

$$D_{\text{O}_2}^{\text{eff}} = D_{\text{O}_2} (\epsilon^{\text{eff}})^{\tau} \quad (5)$$

$$\epsilon^{\text{eff}} = \epsilon (1 - s)$$

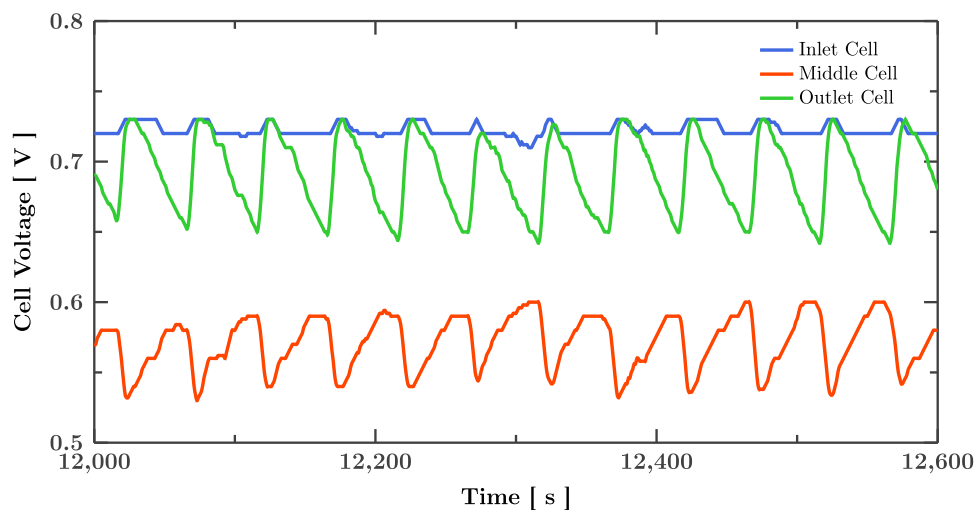


Fig. 3. Voltage drop of various cells during cathode dead-end operation.

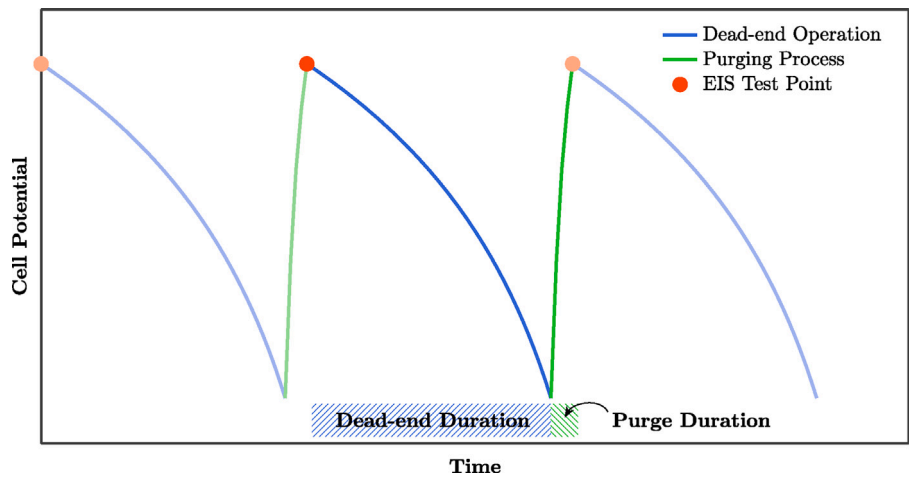


Fig. 4. Schematic of the transient cell potential profile during dead-end mode operation and purging process, as well as the point of carrying out EIS test.

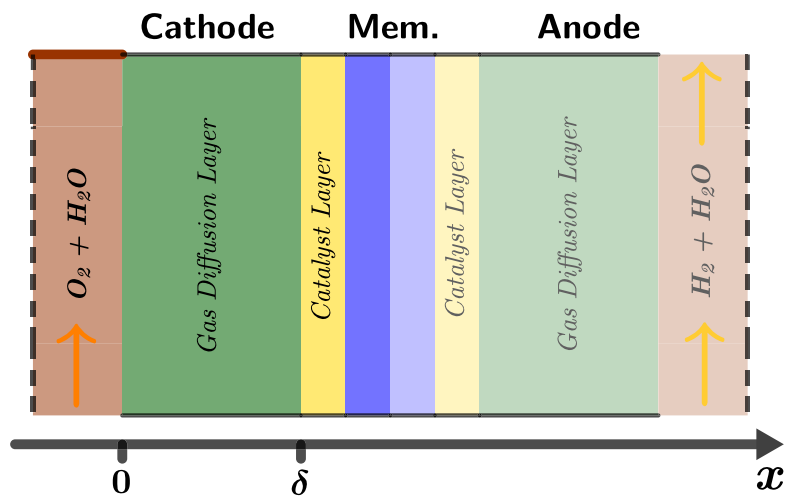


Fig. 5. 1D Schematic of the PEMFC in dead-end mode operation. The washout color points to the 2nd hypothesis which refers to neglecting the anode side due to fast kinetics and also open-end operation.

the value of tortuosity is usually taken to be equal to 1.5 [23]. Also, the diffusivity of the oxygen species in channel region (D_{O_2}) is computed as a function of operating temperature and pressure relative to their reference values [24]:

$$D_{O_2} = D_{O_2}^0 \left(\frac{T}{T^0} \right)^{1.5} \left(\frac{P^0}{P} \right) \quad (6)$$

Based on the ideal gas law, the oxygen concentration term in Eq. (4) would be possible to be substituted by gas pressure:

$$P_{O_2} V = N_{O_2} RT \rightarrow C_{O_2} = \frac{N_{O_2}}{V} = \frac{P_{O_2}}{RT} \quad (7)$$

As a result, Eq. (4) is rearranged as:

$$\frac{dP_{O_2}}{dt} = D_{O_2}^{\text{eff}} \frac{d^2 P_{O_2}}{dx^2} \quad (8)$$

To solve this equation, we need two boundary conditions [21]:

1. As the inlet flow of the cathode is saturated, the oxygen pressure at the channel/GDL interface is equal to:

$$P_{O_2}(0) = P^{\text{in}} - P_{H_2O}^{\text{sat}} \quad (9)$$

2. On the other side, the Faradic current determines the oxygen flow rate from GDL to the catalyst layer, based on the Faraday's law:

$$D_{O_2}^{\text{eff}} \frac{dP_{O_2}}{dx}(\delta) = -\frac{RT}{4F} j_F \quad (10)$$

3.1.3. Charge balance equation

From an electrochemical point of view, two distinct phenomena occur in a cathode when a PEMFC is subjected to a current. The first one is electrons and protons accumulation at the electrode-electrolyte interface, which is called the “double-layer” effect. The second one is the electrochemical reactions on the active surface area of the catalyst layer. As a result, the total current can be divided into a capacitive current due to a double-layer effect and a Faradic current due to the electrochemical reactions:

$$j_T S_e = j_C S_e + j_F S_{\text{act}} \quad (11)$$

As indicated in the above equation, although the produced liquid water does not affect the capacitive current, the electrochemical reactions will be negatively influenced because of water flooding and consequent deficiency of available active area [21]. Therefore, by applying Eq. (2) to the above relation, the total current density will be:

$$j_T = C_{dl} \frac{d\eta}{dt} + j_F (1 - s) \quad (12)$$

The Faradic current density and the over-potential of the oxygen reduction reaction taking place at the cathode electrode are associated with each other by Tafel law which holds true for the typical working current densities of a PEMFC [25,26]:

$$j_F = j_{\text{ex}} \left(\frac{P_{O_2}}{P_{O_2}^0} \right)^{\gamma} e^{\left(\frac{\alpha n F}{RT} \eta \right)} \quad (13)$$

in which the terms α and γ represent the charge transfer coefficient and the reaction order, respectively.

The cell potential during the imposed current density then can be obtained using:

$$U = E_{OCV} - R_{\text{ohm}} j_T S_e - \eta \quad (14)$$

where R_{ohm} refers to the ohmic resistance arising from membrane and various layers contacts, and also E_{OCV} is the open circuit potential of the cathode.

3.2. Frequency domain solution

Basically, EIS method involves perturbing a steady-state system by a harmonic excitation signal that is as small as it will not deteriorate the system's linearity. In mathematical notation, the excitation and response signals are expressed through the following complex form:

$$\phi = \bar{\phi} + \tilde{\phi} e^{i\omega t} \quad (15)$$

In the above, $\bar{\phi}$ and $\tilde{\phi}$ are steady-state value and oscillating amplitude of the signals, respectively. Also, we have $i = \sqrt{-1}$ for imaginary component, t for the time and $\omega = 2\pi f$ for the angular velocity in which f is the frequency. Inserting Eq. (15) into the governing equations results in a transient system of equations based on the perturbed variables. The Physical impedance model then can be derived considering three consecutive steps: linear approximation of the transient system by applying a first-order Taylor series expansion to it, subtraction of the steady-state parts from the linearized system, and finally, performing Fourier transform to the obtained equations [26–28]. This procedure ends in a complex boundary value problem (BVP) that solving it gives the impedance of the system according to the definition below:

$$Z = -\frac{d\tilde{U}}{d\tilde{j}_T} \quad (16)$$

We start the above procedure by first incorporating Eq. (15) into Eq. (14), which results in:

$$\bar{U} + \tilde{U} = E_{OCV} - R_{\text{ohm}} (j_T + \tilde{j}_T) S_e - (\bar{\eta} + \tilde{\eta}) \quad (17)$$

It should be noted that the excitation signal will not influence the values of the geometrical and physical properties. Subtracting the steady-state part, we get to the following equation for the perturbation variables of the excitation and response signals:

$$\tilde{U} = -R_{\text{ohm}} \tilde{j}_T S_e - \tilde{\eta} \quad (18)$$

One can calculate the impedance of the system by differentiating Eq. (18) with respect to the perturbed current density (\tilde{j}_T):

$$Z = -\frac{d\tilde{U}}{d\tilde{j}_T} = R_{\text{ohm}} S_e + \frac{d\tilde{\eta}}{d\tilde{j}_T} \quad (19)$$

To calculate the second term on the right hand side of Eq. (19), we first combine Eqs. (3) and (11) to derive the following relation:

$$j_T = C_{dl} \frac{d\eta}{dt} + A \frac{ds}{dt} \quad (20)$$

Based on the complex notation (15), the perturbed form of a signal's time derivative can be obtained as:

$$\frac{d\phi}{dt} = \frac{d\tilde{\phi}}{dt} = (i\omega) \tilde{\phi} \quad (21)$$

Therefore, perturbing Eq. (20) results in:

$$\tilde{j}_T = C_{dl} (i\omega) \tilde{\eta} + A (i\omega) \tilde{s} \quad (22)$$

where as a consequence, its derivative with respect to perturbed current density (\tilde{j}_T) gives the unknown:

$$\frac{d\tilde{j}_T}{d\tilde{\eta}} = C_{dl} (i\omega) + A (i\omega) \frac{d\tilde{s}}{d\tilde{\eta}} \quad (23)$$

To determine the above equation, we decompose its second term utilizing the chain rule in derivatives:

$$\frac{d\tilde{s}}{d\tilde{\eta}} = \frac{d\tilde{s}}{d\tilde{j}_F} \frac{d\tilde{j}_F}{d\tilde{\eta}} \quad (24)$$

Defining the following relations for saturation and Faradic impedances, respectively:

$$\begin{aligned} Z_{\text{sat}} &= \frac{d\tilde{s}}{d\tilde{j}_F} \\ Z_F &= \frac{d\tilde{\eta}}{d\tilde{j}_F} \end{aligned} \quad (25)$$

Eq. (23) can be rearranged as:

$$\frac{d\tilde{j}_T}{d\tilde{\eta}} = C_{dl}(i\omega) + A(i\omega) \frac{Z_{sat}}{Z_F} \quad (26)$$

In the next two sections, we will seek a solution for the values of the above expressions.

3.2.1. Saturation impedance

Analogous to Ref. [29], it is possible to introduce a definition for the saturation impedance as below:

$$Z_{sat} = \frac{d\tilde{s}}{d\tilde{j}_T} \quad (27)$$

However, it should be noted that since the capacitive current is not affected by the liquid water at the reaction site (Eq. (11)), mathematically, we will have:

$$\frac{d\tilde{j}_C}{d\tilde{s}} = 0 \rightarrow \frac{d\tilde{s}}{d\tilde{j}_T} = \frac{d\tilde{s}}{d\tilde{j}_F} \quad (28)$$

In order to determine the value of the saturation impedance, we must perturb Eq. (1) by inserting Eq. (15) into it:

$$A \frac{d(\tilde{s} + \bar{s})}{dt} = (\tilde{j}_F + \bar{j}_F) [1 - (\tilde{s} + \bar{s})] \quad (29)$$

Then by removing the nonlinear and the steady-state terms as well as applying Fourier transform, we will have:

$$A(i\omega)\tilde{s} = (1 - \bar{s})\tilde{j}_F - \bar{j}_F\tilde{s} \rightarrow \frac{d\tilde{s}}{d\tilde{j}_F} = \frac{(1 - \bar{s})}{\tilde{j}_F + A(i\omega)} \quad (30)$$

It should be clarified that due to the transient governing equations of the system in dead-end mode, the steady-state condition refers to the operation of the PEMFC in the corresponding open end mode, which is before closing the purge valve.

3.2.2. Faradic impedance

For computing the inverse of Faradic impedance, we excite Eq. (13) and then get its derivative with respect to the perturbed over-potential ($\tilde{\eta}$):

$$\begin{aligned} \tilde{j}_F &= k \frac{\alpha}{b} \bar{P}_{O_2} e^{\left(\frac{\alpha\tilde{\eta}}{b}\right)} \tilde{\eta} + k \gamma \bar{P}_{O_2}^{(\gamma-1)} e^{\left(\frac{\alpha\tilde{\eta}}{b}\right)} \tilde{P}_{O_2} \\ &\rightarrow \frac{d\tilde{j}_F}{d\tilde{\eta}} = \frac{\alpha}{b} \tilde{j}_F \left(1 + \frac{\gamma}{\alpha} \frac{\tilde{P}_{O_2}}{\bar{P}_{O_2}} \frac{d\tilde{P}_{O_2}}{d\tilde{\eta}}\right) \end{aligned} \quad (31)$$

In the above equations, parameters b and k stand for:

$$b = \frac{RT}{4F}, \quad k = \frac{j_{ex}}{\left(\bar{P}_{O_2}^0\right)^\gamma} \quad (32)$$

Following the same pattern of Eq. (24) in breaking down the last term of Eq. (31), it can be rewritten as:

$$\frac{d\tilde{P}_{O_2}}{d\tilde{\eta}} = \frac{d\tilde{P}_{O_2}}{d\tilde{j}_F} \frac{d\tilde{j}_F}{d\tilde{\eta}} \rightarrow \frac{d\tilde{j}_F}{d\tilde{\eta}} = \frac{\alpha}{b} \tilde{j}_F \frac{1}{\left(1 - \gamma \tilde{j}_F \frac{1}{\bar{P}_{O_2}} \frac{d\tilde{P}_{O_2}}{d\tilde{j}_F}\right)} \quad (33)$$

To calculate the unknown derivative to the right of the above relation, we need to utilize the oxygen species equation and its boundary conditions. Therefore, by combining Eqs. (5) and (15) with Eqs. (8)–(10) and performing the standard procedure of linearization and Fourier transform, the following system of differential equations will be acquired:

$$\begin{aligned} \frac{d\tilde{P}_{O_2}}{dt} &= \bar{D}_{O_2}^{\text{eff}} \left(\frac{d^2\tilde{P}_{O_2}}{dx^2} - \frac{1.5}{(1 - \bar{s})} \frac{d^2\tilde{P}_{O_2}}{dx^2} \tilde{s} \right) \\ \bar{D}_{O_2}^{\text{eff}} \left(\frac{d\tilde{P}_{O_2}}{dx}(\delta) - \frac{1.5}{(1 - \bar{s})} \frac{d\tilde{P}_{O_2}}{dx}(\delta) \tilde{s} \right) &= -b \tilde{j}_F \\ \tilde{P}_{O_2}(0) &= 0 \end{aligned} \quad (34)$$

the solution of which consists of determining the first and second steady-state pressure gradients. To do so we require to solve Eq. (8) without time derivative:

$$\bar{D}_{O_2}^{\text{eff}} \frac{d^2\tilde{P}_{O_2}}{dx^2} = 0 \rightarrow \tilde{P}_{O_2}(x) = px + q \quad (35)$$

Introducing the related boundary conditions in steady-state to Eq. (35), the constants can be obtained:

$$\begin{aligned} x = 0 &\rightarrow \tilde{P}_{O_2}(0) = q = P^{\text{in}} - P_{H_2O}^{\text{sat}} \\ x = \delta &\rightarrow \frac{d\tilde{P}_{O_2}}{dx}(\delta) = p = -\frac{b}{\bar{D}_{O_2}^{\text{eff}}} \tilde{j}_F \end{aligned} \quad (36)$$

In the foregoing equations, $\bar{D}_{O_2}^{\text{eff}}$ denotes for the value of oxygen diffusivity in steady-state:

$$\bar{D}_{O_2}^{\text{eff}} = D_{O_2} [\varepsilon (1 - \bar{s})]^{1.5} \quad (37)$$

Applying the achieved expressions for steady-state condition to those for perturbed system (Eq. (34)), the updated form of the system of differential equations will be:

$$\bar{D}_{O_2}^{\text{eff}} \frac{d^2\tilde{P}_{O_2}}{dx^2} = (i\omega) \tilde{P}_{O_2} \quad (38)$$

$$\bar{D}_{O_2}^{\text{eff}} \frac{d\tilde{P}_{O_2}}{dx}(\delta) = -b \left(1 + 1.5 \frac{\tilde{j}_F}{\tilde{j}_F + A(i\omega)} \right) \tilde{j}_F \quad (39)$$

Eq. (38) is a second-order homogeneous linear differential equation with constant coefficients which its general solution is of the form:

$$\tilde{P}_{O_2}(x, \omega) = A(\omega) \cosh \left(\sqrt{\frac{(i\omega)}{\bar{D}_{O_2}^{\text{eff}}}} x \right) + B(\omega) \sinh \left(\sqrt{\frac{(i\omega)}{\bar{D}_{O_2}^{\text{eff}}}} x \right) \quad (40)$$

This general solution has two indefinite functions of angular frequency to be specified with the associated boundary conditions of the perturbed system.

- At the interface of the channel and GDL ($x = 0$):

$$x = 0 \rightarrow A(\omega) = \tilde{P}_{O_2}(0) = 0 \quad (41)$$

- At the interface of the GDL and catalyst layer ($x = \delta$), due to Eq. (39):

$$\begin{aligned} x = \delta &\rightarrow B(\omega) = -b \left(1 + 1.5 \frac{\tilde{j}_F}{\tilde{j}_F + A(i\omega)} \right) \\ &\times \frac{\tilde{j}_F}{\sqrt{(i\omega) \bar{D}_{O_2}^{\text{eff}}} \cosh \left(\sqrt{\frac{(i\omega)}{\bar{D}_{O_2}^{\text{eff}}}} \delta \right)} \end{aligned} \quad (42)$$

Now it is possible to establish the expression for the inverse of Faradic impedance by at first incorporating Eqs. (41) and (42) into Eq. (40) and then differentiating it with respect to perturbed Faradic current density \tilde{j}_F :

$$\frac{d\tilde{P}_{O_2}}{d\tilde{j}_F} = -b \left(1 + 1.5 \frac{\tilde{j}_F}{\tilde{j}_F + A(i\omega)} \right) \frac{\tanh \left(\sqrt{\frac{(i\omega)}{\bar{D}_{O_2}^{\text{eff}}}} \delta \right)}{\sqrt{(i\omega) \bar{D}_{O_2}^{\text{eff}}}} \quad (43)$$

and secondly, calculating the steady-state distribution of oxygen pressure at the reaction site ($x = \delta$)

$$\tilde{P}_{O_2}(\delta) = -\frac{b\tilde{j}_F}{\bar{D}_{O_2}^{\text{eff}}} \delta + (P^{\text{in}} - P_{H_2O}^{\text{sat}}) \quad (44)$$

Integrating the above derived relations with Eq. (33) would result in:

$$\frac{d\tilde{j}_F}{d\tilde{\eta}} = \frac{\alpha}{b} \tilde{j}_F$$

$$\left(1 - \gamma \frac{j_F}{\frac{1}{\frac{b j_F}{\bar{D}_{O_2}^{\text{eff}}} \delta + (P^{\text{in}} - P_{H_2O}^{\text{sat}})}} \right) \left[-b \left(1 + 1.5 \frac{j_F}{j_F + A(i\omega)} \right) \frac{\tanh \left(\sqrt{\frac{(i\omega)}{\bar{D}_{O_2}^{\text{eff}}} \delta} \right)}{\sqrt{(i\omega) \bar{D}_{O_2}^{\text{eff}}}} \right] \quad (45)$$

3.3. Total impedance calculation

For simplifying the representation of the total impedance expression, we, at first, try to concise Eq. (45) by following definitions:

$$\begin{aligned} R_{ct} &= \frac{b}{\alpha} \frac{1}{j_F} \\ R_{O_2} &= \frac{b}{\alpha} \frac{\gamma}{\left[-\frac{b j_F}{\bar{D}_{O_2}^{\text{eff}}} \delta + (P^{\text{in}} - P_{H_2O}^{\text{sat}}) \right]} = \frac{b}{\alpha} \frac{\gamma}{\bar{P}_{O_2}(\delta)} \\ Z_{\text{diff}, O_2} &= \left[b \left(1 + 1.5 \frac{j_F}{j_F + A(i\omega)} \right) \frac{\tanh \left(\sqrt{\frac{(i\omega)}{\bar{D}_{O_2}^{\text{eff}}} \delta} \right)}{\sqrt{(i\omega) \bar{D}_{O_2}^{\text{eff}}}} \right] = -\frac{d\tilde{P}_{O_2}}{d\tilde{j}_F} \end{aligned} \quad (46)$$

In the preceding expressions, R_{ct} is the charge transfer resistance, R_{O_2} is the low-frequency limit of resistance, and Z_{diff, O_2} is the oxygen diffusion impedance. Subsequently, Eq. (45) will take the following form:

$$\frac{1}{Z_F} = \frac{1}{R_{ct} + R_{O_2} Z_{\text{diff}, O_2}} \quad (47)$$

Now, based on the Eq. (19), the total impedance can be derived as follows:

$$Z = R_{\text{ohm}} S_e + \frac{d\tilde{\eta}}{d\tilde{j}_T} = R_{\text{ohm}} S_e + \frac{1}{C_{dl}(i\omega) + \left(\frac{Z_{\text{sat}}}{R_{ct} + R_{O_2} Z_{\text{diff}, O_2}} \right) A(i\omega)} \quad (48)$$

4. Results and discussion

4.1. Validation of the physical impedance model

Table 2 lists the physical constants and the cell parameters employed in the developed model. The unknown parameters, which cannot be obtained by direct measurements, are approximated using a fitting technique that reduces the model's error to the noise level of the test. Due to the nonlinearity of the governing equations with regard to the unknowns, the nonlinear variant of the least-squares approach is used for this purpose. This approach tries to minimize an objective function consisting of the weighted sum of the quadratic difference between model results and experimental data (Eq. (49)).

$$\text{Model's Error} = \min \left(\sum_{k=1}^m W_k (Y_{\text{Data}} - \hat{Y}_{\text{Model}})_k^2 \right) \quad (49)$$

The primary issues with the aforementioned optimization problem are the suitable number of unknown parameters and the correct selection of their initial values. This may lead to a challenge for the accuracy or even convergence of the obtained solution. To overcome the mentioned issues, the former is addressed using a two-step fitting strategy in which the unknown parameters are separated into two groups, one of which is estimated using polarization curves and the other using impedance diagrams. The latter is handled using a graphical technique that estimates unknown parameters based on experimental polarization

Table 2

Physical constants and cell parameters of the model.

| Parameter | Symbol | Unit | Value |
|------------------------|----------------|-------------------------------------|----------|
| Electrode surface area | S_e | m ² | 0.05 |
| GDL thickness | δ_{GDL} | m | 325e-6 |
| GDL free porosity | ϵ | – | 0.52 |
| GDL tortuosity factor | τ | – | 1.5 |
| Faraday's constant | F | C mol ⁻¹ | 96485 |
| Universal gas constant | R | J K ⁻¹ mol ⁻¹ | 8.314 |
| Open circuit potential | E_{OCV} | V | 1.07 |
| Oxygen diffusivity | D_{O_2} | m ² s ⁻¹ | 1.806e-5 |
| Relative humidity | RH | – | 100% |
| Water density | ρ_{H_2O} | Kg m ⁻³ | 1000 |
| Water molar mass | M_{H_2O} | Kg mol ⁻¹ | 0.018 |

and impedance data characteristics. As a result, the combined use of the graphical method [30] and the two-step fitting approach [31] has been presented in this work.

The model's unknown parameters are included in Table 3, along with their initial value regression and fitting methods. According to the graphical method, the exchange current density can be determined around the OCV point of the polarization curve by using a linear form of the Butler–Volmer equation (Eq. (50)). In addition, the internal resistance is approximated by the high-frequency limit of the real part of the impedance diagram from the Nyquist plot [19]. The capacitance of the double-layer is estimated using the top point of the semicircle of the impedance diagram (Eq. (51)). Initial values of α and γ are chosen based on the symmetrical activation barrier and one half reaction order assumptions [25,32].

$$j_{ex} = \frac{RT}{F} \frac{j_F}{\eta} \quad (50)$$

$$C_{dl} = \frac{1}{2\pi f_{\text{top}} R_{ct}} \quad (51)$$

Using the set of unknown parameters α, γ, j_{ex} , the steady-state model was fitted to the experimental data of the polarization curves in the first step of the fitting procedure (Fig. 6). It is worth mentioning that due to the invalidity of the Tafel relation near the OCV, the first point has been excluded from the fitting process. The values presented in Table 4 for the fitting parameters are the obtained averages of the multiple code execution results along with their 95% confidence intervals and fall within the range of values reported in the literature [33,34]. It should be noted that to compare the obtained charge transfer coefficient to those in other sources, its values must be multiplied by n , the number of electrons participating in the electrode reaction (Eq. (13)). Among the first set of the fitting parameters, the exchange current density has the most changes since this parameter is affected by both pressure and temperature variables. Finally, a value between 0.5 and 1 is also considered valid for the reaction order of the oxygen reduction at the cathode side [35]. According to Fig. 6, the obtained values produced a very good agreement between model and experimental data and were considered valid and treated as fixed parameters for the next step.

Before performing the second step of the fitting procedure, the quality of the EIS experimental data must be evaluated to determine whether its validity requirements (causality, stability, and linearity) are fulfilled. This is especially crucial for the current experiment since the fuel cell operates in a dead-end mode, and the system will be inherently transient in such a condition. Consequently, the EIS experimental data were compared to the Kramers–Kronig transformed ones, yielding qualitatively identical results (Fig. 7). Moreover, the sum of the squares of the relative residuals (χ^2) provides a quantitative measure of the data's quality and the amount of noise contained. Acceptable values are those of the order 10⁻⁵ or less [26]. The linear form of the Kramers–Kronig technique developed by Boukamp [36] is employed in this work. The

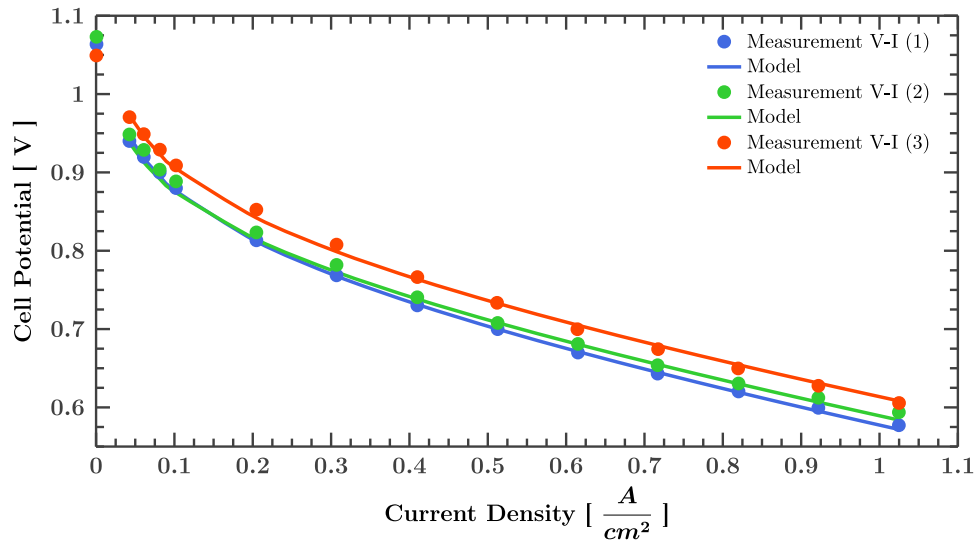


Fig. 6. Polarization curves at different operating conditions: model (solid lines) and measurement (data points).

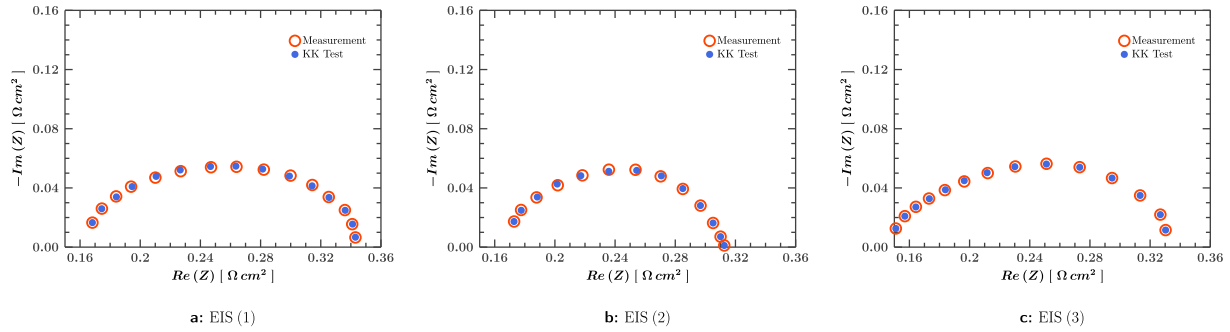


Fig. 7. Kramers-Kronig validation test results of the EIS experimental data.

Table 3

List of unknown parameters, initialization and fitting methodology.

| Parameter | Symbol | Initialization | Fitting |
|-----------------------------|-----------|--|---------|
| Charge transfer coefficient | α | symmetrical activation barrier | V-I |
| Reaction order | γ | one half reaction order | |
| Exchange current density | j_{ex} | linear form of BV equation around OCV | |
| Internal resistance | R_{ohm} | high frequency limit of the Nyquist plot | EIS |
| Double-layer capacitance | C_{dl} | top point of Nyquist plot semicircle | |
| Liquid saturation | \bar{s} | repeating with random values | |

Table 4

Obtained values of unknown parameters through fitting the steady-state model to V-I test measurements.

| Test num. | α (-) | γ (-) | j_{ex} (A cm ⁻²) |
|---------------|-------------------|-----------------|--------------------------------|
| V-I (1) | 0.098 ± 0.002 | 0.81 ± 0.07 | 0.0069 ± 0.0003 |
| V-I (2) | 0.109 ± 0.002 | 0.76 ± 0.08 | 0.0055 ± 0.0006 |
| V-I (3) | 0.103 ± 0.003 | 0.85 ± 0.07 | 0.0203 ± 0.0004 |
| Average | 0.103 | 0.81 | 0.0094 |
| St. deviation | 4% | 5% | 61% |

Table 5

Obtained values of unknown parameters through fitting the impedance model to EIS test measurements.

| Test num. | R_{ohm} (Ω cm ²) | C_{dl} (F cm ⁻²) | \bar{s} (-) | χ^2 (-) |
|---------------|--------------------------------|--------------------------------|-------------------|--------------|
| EIS (1) | 0.156 ± 0.003 | 0.0079 ± 0.0004 | 0.385 ± 0.014 | $5.3e^{-6}$ |
| EIS (2) | 0.158 ± 0.003 | 0.0076 ± 0.0007 | 0.398 ± 0.012 | $7.2e^{-6}$ |
| EIS (3) | 0.149 ± 0.001 | 0.0127 ± 0.0004 | 0.472 ± 0.009 | $1.5e^{-6}$ |
| Average | 0.155 | 0.0109 | 0.418 | — |
| St. deviation | 3% | 25% | 9% | — |

results confirm the validity of the experimental data in the frequency range of interest (Table 5).

In the second step, the acquired fixed parameters and the initial values of the remaining unknown parameters were substituted in the

physical impedance model (Eq. (48)). Consequently, we only used three parameters R_{ohm} , C_{dl} , \bar{s} to fit the experimental EIS data at this point. Due to the complex nature of the impedance data, the complex nonlinear least squares (CNLS) approach was used to concurrently fit

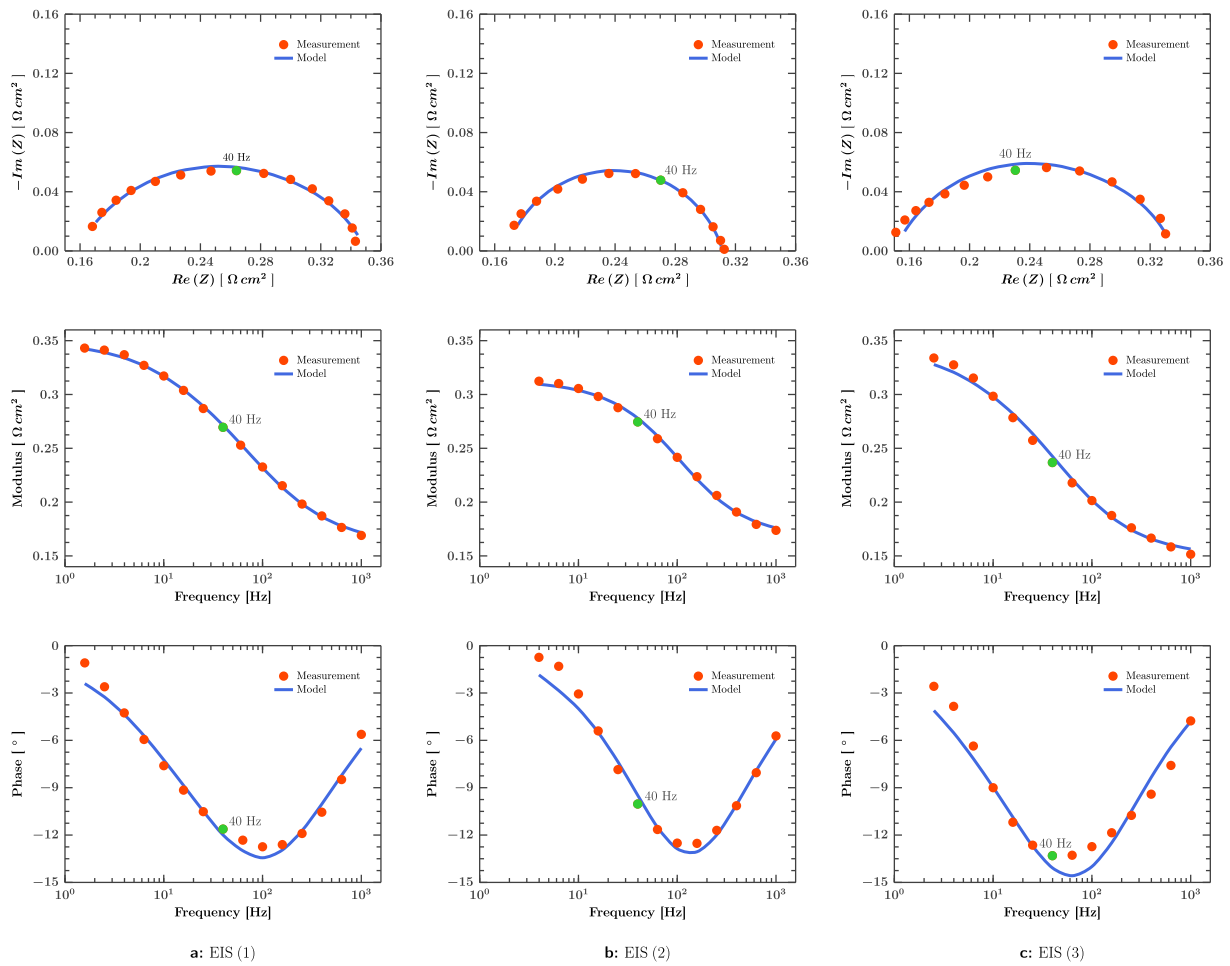


Fig. 8. Electrochemical impedance diagrams at different operating conditions: model (solid lines) and measurement (data points).

the real and imaginary parts of the data to the model. It should be noticed that a CPE element substituted the C_{dl} to account for the spatial distribution of the double-layer capacitance in the electrode, which is a common task in fitting impedance models to experimental data. Fig. 8 demonstrates the results via comparative diagrams in the form of Nyquist and Bode (modulus and phase) plots. A totally good agreement has been found between the model (solid lines) and measurements (data points). To assist with comparing, the position of the 40 Hz frequency point was highlighted on the diagrams.

Table 5 demonstrates the variation of the second set of fitting parameters due to varying operating conditions. According to the results, it is evident that in the dead-end operating mode, there is always a large amount of liquid water permanently present in the fuel cell, which intensifies the importance of water management discussion in this type of operation. This results confirms the previous findings in the related literature [21]. Also, the double-layer capacitance and ohmic resistance values increased and decreased, respectively, with varying operating conditions. The increased operating temperature influences the saturation level by significantly improving the fuel cell performance (increased exchange current density) and hence producing more liquid water. As a result, the enhanced membrane hydration causes the reduction of the ohmic resistance. The variation of double-layer capacitance obeys the Gouy–Chapman–Stern model and increases with temperature [37], but investigating its details is beyond the scope of this article.

4.2. Effect of liquid water saturation on PEMFC performance

4.2.1. Time domain analysis

Solving Eq. (3) in the time domain leads to the following relation for saturation variation during the dead-end operation of the fuel cell:

$$s(t) = 1 - (1 - \bar{s}) e^{-t \frac{j_F}{A}} \quad (52)$$

In the above equation, to draw a saturation profile at any current density, it is only necessary to specify the parameter \bar{s} . Its value has been determined by fitting to the EIS data in the previous section (Table 5). Fig. 9 shows the saturation profile during dead-end operation and purge valve opening intervals for test (1) operating condition. It should be noted that Eq. (52) gives the saturation profile during a dead-end operation, and the diagram of the purge valve opening section is calculated in terms of exponential behavior between the start and end points. The accumulation of liquid water affects the dead-end mode performance of a PEMFC in two ways. Firstly, it reduces the active surface area available for the reaction by covering the catalyst packages and preventing oxygen access to them. Secondly, liquid water fills the pores of the GDL porous medium and makes it difficult for oxygen gas to reach the catalyst layer, resulting in a reduced effective diffusion coefficient.

Consequently, over time and with increasing liquid water saturation, the PEMFC's performance deteriorates, and the voltage drops.

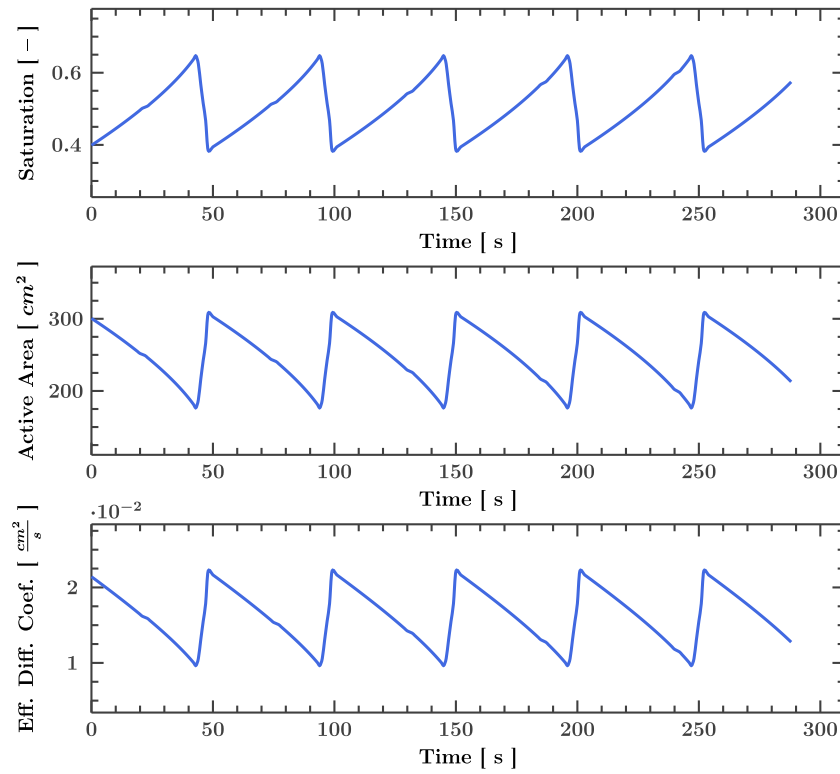


Fig. 9. Time evolution of saturation (top), active area (middle) and effective diffusion coefficient (bottom) profiles during dead-end operation and purge valve opening intervals for test (1) operating condition.

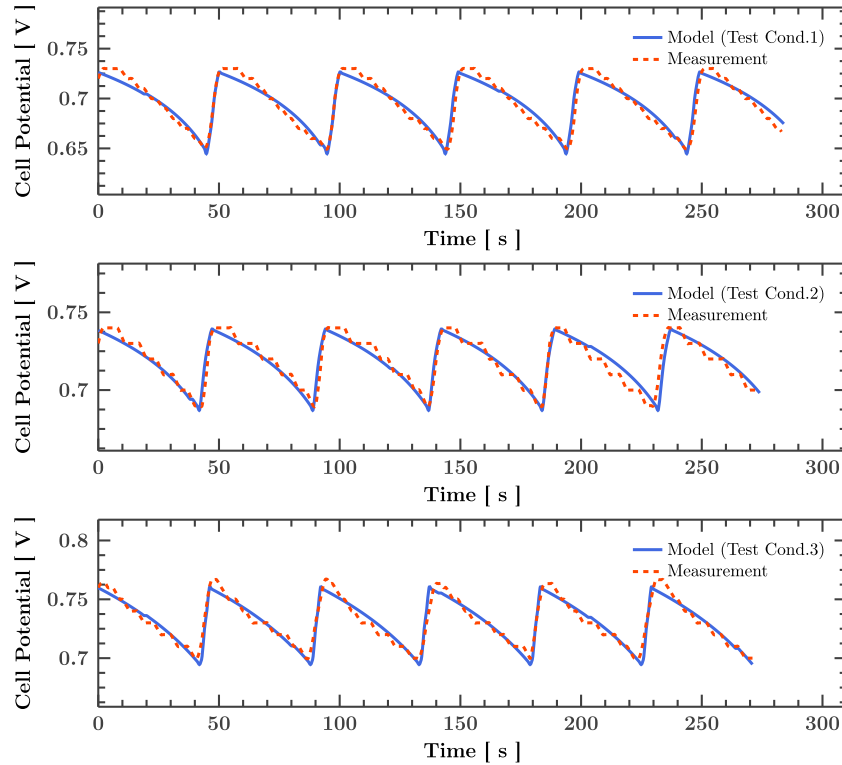


Fig. 10. Cell potential transients for different operating conditions: model (solid lines) and measurement (dash lines).

Then, opening the purge valve is required after a duration to drain the accumulated water, recover the voltage, and improve the cell

performance. Fig. 10 illustrates the cell potential transients for all three test conditions through both the developed model and measurements.

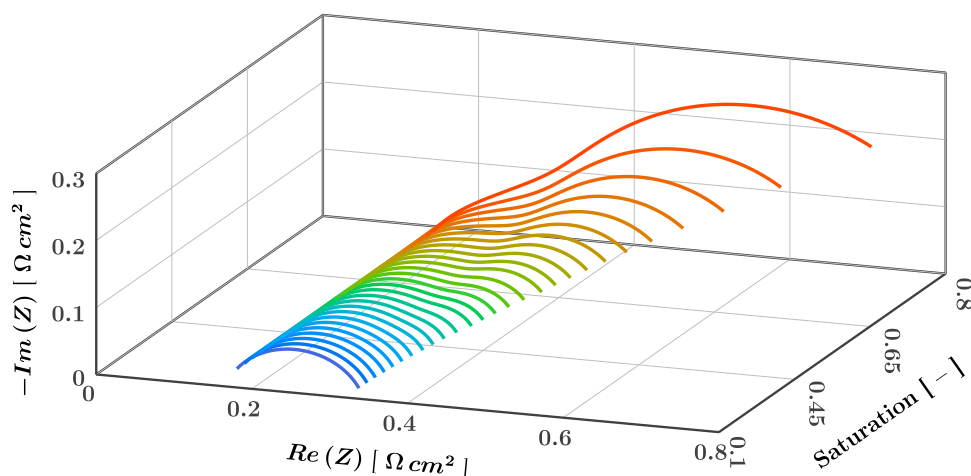


Fig. 11. 3D plot of the effect of saturation level variation on the impedance diagram under test EIS (1) operating condition.

Additionally, the good agreement across the plots also supports the model's adequate validity in the time domain.

4.2.2. Frequency domain analysis

Fig. 11 depicts the effect of saturation level variations on the EIS diagram under test EIS (1) operating condition with all other parameters held constant. In fact, it provides the sensitivity analysis of the impedance model with respect to liquid water saturation. It should be emphasized that conducting experiments at high volumes of accumulated water could be detrimental to the fuel cell's health condition because its dead-end operation under such conditions can easily cause severe reactants starvation, which may end in membrane degradation or even failure. As shown in the figure, the change in liquid water saturation initially affects the high-frequency arc and increases the charge transfer resistance. This is due to the catalyst layer flooding phenomenon that reduces the catalyst layer's active surface area [38]. For higher amounts of saturation level, the mass transfer semicircle appears gradually as a result of the filled pores of GDL porous medium and reduced diffusion of oxygen. The growth of the low-frequency arc with increasing saturation level implicitly expresses the effect of the flow channel on the impedance diagram. In fact, more liquid water builds up towards the channel output, which severely confines the mass transfer. The resultant oxygen starvation occurring near the end of the channel causes the low-frequency semicircle to enlarge significantly. Therefore, although the effects along the flow channel are not explicitly incorporated in the current model, Fig. 11 can be anticipated to qualitatively demonstrate how the local impedance varies in the flow channel direction.

5. Conclusion

In this study, a novel analytical model for predicting the PEMFC impedance in a dead-end operating mode is proposed, which incorporates the influence of liquid water accumulation on the cathode by employing a transient equation of the saturation level. The results of the developed model were assessed against the V-I and EIS measurements through a two-step fitting procedure and were satisfactorily verified. According to the findings, it was found that: 1. A considerable volume of liquid water accumulates permanently in the fuel cell due to the dead-end operation. Therefore, water management becomes much more crucial. 2. Accumulation of liquid water impacts both the high and low-frequency arcs in the impedance of a dead-end PEMFC. Firstly, it increases the charge transfer resistance by covering the catalyst packages and hence reducing the active area of the catalyst layer. Secondly, the filled pores of the GDL porous medium confine the oxygen diffusion and cause the mass transfer semicircle to appear and

grow. The analytical nature of the presented impedance model causes its low computational cost and makes it a suitable tool for applications such as fault detection and prognostics in PEMFCs with a dead-end operation.

CRediT authorship contribution statement

Majid Shateri: Conception and design of study, Acquisition of data, Analysis and/or interpretation of data, Writing – original draft, Writing – review & editing. **Farschad Torabi:** Conception and design of study, Writing – review & editing.

Declaration of competing interest

The authors declare that they have no known competing financial interests or personal relationships that could have appeared to influence the work reported in this paper.

Data availability

The data that has been used in the research is represented in the form of the plot figures.

Acknowledgments

All authors approved the version of the manuscript to be published.

References

- [1] I. Staffell, D. Scamman, A. Velazquez Abad, P. Balcombe, P.E. Dodds, P. Ekins, N. Shah, K.R. Ward, The role of hydrogen and fuel cells in the global energy system, *Energy Environ. Sci.* 12 (2) (2019) 463–491, <http://dx.doi.org/10.1039/c8ee01157e>.
- [2] J.M. Thomas, P.P. Edwards, P.J. Dobson, G.P. Owen, Decarbonising energy: The developing international activity in hydrogen technologies and fuel cells, *J. Energy Chem.* 51 (2020) 405–415, <http://dx.doi.org/10.1016/j.jechem.2020.03.087>.
- [3] A. Chapman, D.H. Nguyen, H. Farabi-Asl, K. Itaoka, K. Hirose, Y. Fujii, Hydrogen penetration and fuel cell vehicle deployment in the carbon constrained future energy system, *IET Electr. Syst. Transp.* 10 (4) (2020) 409–416, <http://dx.doi.org/10.1049/iet-est.2020.0014>.
- [4] J.C. Kurnia, A.P. Sasmito, T. Shamim, Advances in proton exchange membrane fuel cell with dead-end anode operation: A review, *Appl. Energy* 252 (2019) 113416, <http://dx.doi.org/10.1016/j.apenergy.2019.113416>.
- [5] A. Chiche, G. Lindbergh, I. Stenius, C. Lagergren, Design of experiment to predict the time between hydrogen purges for an air-breathing PEM fuel cell in dead-end mode in a closed environment, *Int. J. Hydrogen Energy* 46 (26) (2021) 13806–13817, <http://dx.doi.org/10.1016/j.ijhydene.2021.01.035>.

- [6] J.W. Choi, Y.-S. Hwang, J.-H. Seo, D.H. Lee, S.W. Cha, M.S. Kim, An experimental study on the purge characteristics of the cathodic dead-end mode PEMFC for the submarine or aerospace applications and performance improvement with the pulsation effects, *Int. J. Hydrogen Energy* 35 (8) (2010) 3698–3711, <http://dx.doi.org/10.1016/j.ijhydene.2010.01.133>.
- [7] M. Rahimi-Esbo, A. Ramiar, A. Ranjbar, E. Alizadeh, Design, manufacturing, assembling and testing of a transparent PEM fuel cell for investigation of water management and contact resistance at dead-end mode, *Int. J. Hydrogen Energy* 42 (16) (2017) 11673–11688, <http://dx.doi.org/10.1016/j.ijhydene.2017.02.030>.
- [8] B. Chen, J. Wang, T. Yang, Y. Cai, C. Zhang, S.H. Chan, Y. Yu, Z. Tu, Carbon corrosion and performance degradation mechanism in a proton exchange membrane fuel cell with dead-ended anode and cathode, *Energy* 106 (2016) 54–62, <http://dx.doi.org/10.1016/j.energy.2016.03.045>.
- [9] M.R. Esbo, A. Ranjbar, S. Rahgoshay, Analysis of water management in PEM fuel cell stack at dead-end mode using direct visualization, *Renew. Energy* 162 (2020) 212–221, <http://dx.doi.org/10.1016/j.renene.2020.06.078>.
- [10] E. Alizadeh, M. Khorshidian, S. Saadat, S. Rahgoshay, M. Rahimi-Esbo, The experimental analysis of a dead-end H_2/O_2 PEM fuel cell stack with cascade type design, *Int. J. Hydrogen Energy* 42 (16) (2017) 11662–11672, <http://dx.doi.org/10.1016/j.ijhydene.2017.03.094>.
- [11] X. Wang, Y. Ma, J. Gao, T. Li, G. Jiang, Z. Sun, Review on water management methods for proton exchange membrane fuel cells, *Int. J. Hydrogen Energy* 46 (22) (2021) 12206–12229, <http://dx.doi.org/10.1016/j.ijhydene.2020.06.211>.
- [12] S. Chevalier, N. Ge, J. Lee, P. Antonacci, R. Yip, M. George, H. Liu, R. Banerjee, M. Fazeli, A. Bazylak, In situ analysis of voltage degradation in a polymer electrolyte membrane fuel cell with a dead-ended anode, *Electrochim. Commun.* 59 (2015) 16–19, <http://dx.doi.org/10.1016/j.elecom.2015.06.009>.
- [13] J.B. Siegel, D.A. McKay, A.G. Stefanopoulou, D.S. Hussey, D.L. Jacobson, Measurement of liquid water accumulation in a PEMFC with dead-ended anode, *J. Electrochem. Soc.* 155 (11) (2008) B1168, <http://dx.doi.org/10.1149/1.2976356>.
- [14] C. Cadet, S. Jemei, F. Druart, D. Hissel, Diagnostic tools for PEMFCs: from conception to implementation, *Int. J. Hydrogen Energy* 39 (20) (2014) 10613–10626, <http://dx.doi.org/10.1016/j.ijhydene.2014.04.163>.
- [15] Q. Meyer, S. Ashton, O. Curnick, T. Reisch, P. Adcock, K. Ronaszegi, J.B. Robinson, D.J. Brett, Dead-ended anode polymer electrolyte fuel cell stack operation investigated using electrochemical impedance spectroscopy, off-gas analysis and thermal imaging, *J. Power Sources* 254 (2014) 1–9, <http://dx.doi.org/10.1016/j.jpowsour.2013.11.125>.
- [16] S. Strahl, A. Husar, J. Riera, Experimental study of hydrogen purge effects on performance and efficiency of an open-cathode Proton Exchange Membrane fuel cell system, *J. Power Sources* 248 (2014) 474–482, <http://dx.doi.org/10.1016/j.jpowsour.2013.09.122>.
- [17] N. Ge, S. Chevalier, D. Muirhead, R. Banerjee, J. Lee, H. Liu, P. Shrestha, K. Fahy, C. Lee, T. Aoki, Y. Tabuchi, A. Bazylak, Detecting cathode corrosion in polymer electrolyte membrane fuel cells in dead-ended anode mode via alternating current impedance, *J. Power Sources* 439 (2019) 227089, <http://dx.doi.org/10.1016/j.jpowsour.2019.227089>.
- [18] S. Asghari, M.R. Ashraf Khorasani, I. Dashti, Investigation of self-humidified and dead-ended anode proton exchange membrane fuel cell performance using electrochemical impedance spectroscopy, *Int. J. Hydrogen Energy* 41 (28) (2016) 12347–12357, <http://dx.doi.org/10.1016/j.ijhydene.2016.05.133>.
- [19] D. Vivona, A. Casalegno, A. Baricci, Validation of a pseudo 2D analytical model for high temperature PEM fuel cell impedance valid at typical operative conditions, *Electrochim. Acta* 310 (2019) 122–135, <http://dx.doi.org/10.1016/j.electacta.2019.04.020>.
- [20] G. Maranzana, J. Mainka, O. Lottin, J. Dillet, A. Lamibrac, A. Thomas, S. Didierjean, A proton exchange membrane fuel cell impedance model taking into account convection along the air channel: On the bias between the low frequency limit of the impedance and the slope of the polarization curve, *Electrochim. Acta* 83 (2012) 13–27, <http://dx.doi.org/10.1016/j.electacta.2012.07.065>.
- [21] P. Moçotéguy, F. Druart, Y. Bultel, S. Besse, A. Rakotondrainibe, Monodimensional modeling and experimental study of the dynamic behavior of proton exchange membrane fuel cell stack operating in dead-end mode, *J. Power Sources* 167 (2) (2007) 349–357, <http://dx.doi.org/10.1016/j.jpowsour.2007.02.028>.
- [22] H. Wang, X.Z. Yuan, H. Li, PEM Fuel Cell Diagnostic Tools, CRC Press/Taylor & Francis, 2012.
- [23] H. Ju, H. Meng, C.-Y. Wang, A single-phase, non-isothermal model for PEM fuel cells, *Int. J. Heat Mass Transfer* 48 (7) (2005) 1303–1315, <http://dx.doi.org/10.1016/j.jheatmasstransfer.2004.10.004>.
- [24] R.B. Bird, W.E. Stewart, E.N. Lightfoot, *Transport Phenomena*, second ed., John Wiley & Sons, 2007.
- [25] A.A. Kulikovskiy, The regimes of catalyst layer operation in a fuel cell, *Electrochim. Acta* 55 (22) (2010) 6391–6401, <http://dx.doi.org/10.1016/j.electacta.2010.06.053>.
- [26] M. Chandesris, C. Robin, M. Gerard, Y. Bultel, Investigation of the difference between the low frequency limit of the impedance spectrum and the slope of the polarization curve, *Electrochim. Acta* 180 (2015) 581–590, <http://dx.doi.org/10.1016/j.electacta.2015.08.089>.
- [27] T. Reshetenko, A.A. Kulikovskiy, Comparison of two physical models for fitting PEM fuel cell impedance spectra measured at a low air flow stoichiometry, *J. Electrochem. Soc.* 163 (3) (2016) F238–F246, <http://dx.doi.org/10.1149/2.0871603jes>.
- [28] A. Baricci, M. Zago, A. Casalegno, Modelling analysis of heterogeneity of ageing in high temperature polymer electrolyte fuel cells: insight into the evolution of electrochemical impedance spectra, *Electrochim. Acta* 222 (2016) 596–607, <http://dx.doi.org/10.1016/j.electacta.2016.11.014>.
- [29] D. Gröbl, J. Janek, W.G. Bessler, Electrochemical pressure impedance spectroscopy (EPIS) as diagnostic method for electrochemical cells with gaseous reactants: A model-based analysis, *J. Electrochem. Soc.* 163 (5) (2016) A599–A610, <http://dx.doi.org/10.1149/2.1041603jes>.
- [30] M.E. Orazem, B. Tribollet, *Electrochemical Impedance Spectroscopy*, John Wiley & Sons, 2017.
- [31] J.R. Vang, F. Zhou, S.J. Andreasen, S.K. Kær, Estimating important electrode parameters of high temperature PEM fuel cells by fitting a model to polarisation curves and impedance spectra, *ECS Trans.* 68 (2015) 13–34, <http://dx.doi.org/10.1149/06803.0013ecst>.
- [32] A.A. Kulikovskiy, *Analytical Modelling of Fuel Cells*, Elsevier, 2010.
- [33] C. Gerling, M. Hanauer, U. Berner, K.A. Friedrich, PEM single cells under differential conditions: full factorial parameterization of the ORR and HOR kinetics and loss analysis, *J. Electrochem. Soc.* 169 (1) (2022) 014503, <http://dx.doi.org/10.1149/1945-7111/ac44ba>.
- [34] A. d'Adamo, M. Haslinger, G. Corda, J. Höflinger, S. Fontanesi, T. Lauer, Modelling methods and validation techniques for CFD simulations of PEM fuel cells, *Processes* 9 (4) (2021) 688, <http://dx.doi.org/10.3390/pr9040688>.
- [35] F. Barbir, *PEM Fuel Cells: Theory and Practice*, Elsevier, 2013.
- [36] B.A. Boukamp, A linear Kronig-Kramers transform test for immittance data validation, *J. Electrochem. Soc.* 142 (6) (1995) 1885–1894, <http://dx.doi.org/10.1149/1.2044210>.
- [37] J.P. Sabawa, A.S. Bandarenka, Applicability of double layer capacitance measurements to monitor local temperature changes at polymer electrolyte membrane fuel cell cathodes, *Results Chem.* 2 (2020) 100078, <http://dx.doi.org/10.1016/j.rechem.2020.100078>.
- [38] J. Zhang, J. Wu, H. Zhang, J. Zhang, *Pem Fuel Cell Testing and Diagnosis*, Elsevier, 2013.